Geomagnetic Pulsations Driving Geomagnetically Induced Currents

M. J. Heyns[1,2], S. I. Lotz[1], C. T. Gaunt[2]

[1]SANSA Space Science, Hermanus
[2]University of Cape Town, Cape Town

Key Points:

- Low-frequency geomagnetic pulsations couple effectively to GICs and need to be taken into account in modelling power network response
- Ps6-type disturbances along with other pulsations are seen at mid-latitudes during intense storms and can drive significant GICs
- dB/dt may not be an appropriate GIC proxy given pulsation driving

Corresponding author: M. J. Heyns, `mheyns@sansa.org.za`

Corresponding author: S. I. Lotz, `slotz@sansa.org.za`

Abstract

Geomagnetically induced currents (GICs) are driven by the geoelectric field induced by fluctuations of Earth's magnetic field. Drivers of intense GICs are often associated with large impulsive events such as coronal mass ejections. To a lesser extent fluctuations from regular oscillations of the geomagnetic field, or geomagnetic pulsations, have also been identified as possible drivers of GICs. In this work we show that these low-frequency pulsations are directly observed in measured GIC data from power networks. Due to the low-pass nature of GICs, Pc5 and lower frequency pulsations drive significant GICs for an extended duration at mid-latitudes. Longer period Ps6-type disturbances apparently not typical of mid-latitudes are seen with GIC amplitudes comparable to the peak GIC at storm sudden commencement. The quasi-ac nature of the sustained pulsation driving affects the power system response and cannot be properly modelled using only dc models. A further consideration is that the often used dB/dt GIC proxy is biased to the sampling rate of the geomagnetic field measurements used. The dB/dt metric does not adequately characterise GIC activity at frequencies in the low ULF range and a frequency weighted proxy akin to geoelectric field should be used instead.

Plain Language Summary

Geomagnetically induced currents (GICs) are naturally occurring currents induced in conductive media, such as the Earth, by fluctuations of the geomagnetic field. When large grounded conductors such as power networks are present, these currents also enter the network and pose serious risk to the stability of the network. In extreme cases, the GICs can result in total network collapse. Particular fluctuations of the local geomagnetic field are geomagnetic pulsations, which occur when the magnetic field lines are perturbed and ring, causing oscillations. These oscillations have not previously been thought to be effective in driving large GICs, but now measured GIC data have shown this is not always the case and the power grid couples particularly well to low-frequency pulsations. Essentially, the power grid acts as an antenna and pulsations have been picked up where not previously expected. Understanding the effectiveness of these pulsations and including them in GIC modelling is vital for protection of the grounded power networks we rely on.

1 Introduction

Research on the occurrence of geomagnetically induced currents (GICs) in power grids is largely focused on the impact of intense sudden perturbations to the geomagnetic field (B-field) such as during sudden commencement and substorms (Kappenman, 2005; Smith et al., 2019). These periods are typically characterised by spike-like peaks with large dB/dt values. Similar peaks are induced in the geoelectric field (E-field) that drives GICs. In the frequency domain, spikes associated with extreme rates of change are broadband driving and mathematically require broadband frequency contributions to be reproduced. GICs on the other hand have been shown to be low-frequency phenomena, with their quasi-dc nature often exploited to model network impacts assuming pure dc driving (Lehtinen & Pirjola, 1985). Most of the GIC power sits below 50 mHz and there is a distinct low-pass filter response (Oyedokun et al., 2020). In short, the B-field has a power spectrum (defined as magnitude squared) that follows a $1/f^m$ relation with frequency, where m is usually between 2 and 4 (Simpson & Bahr, 2005). In the frequency domain, dB/dt or $Bdot$ introduces a high-pass filter of f, i.e. $Bdot(f) = 2\pi i f B(f)$, with the power spectrum following a $1/f^{m-2}$ relation with frequency. The E-field and hence GIC sits between these two power spectrum responses, with the homogeneous earth case $E(f) \propto \sqrt{f} B(f)$. In the homogeneous earth case, the power spectrum of the E-field would follow a $1/f^{m-1}$ relation with frequency, with $m-1 > 0$. The E-field can be seen as either a high-pass filter to the B-field or a low-pass filter to dB/dt. Given that

the B-field response has inherently low-pass characteristics, the E-field also has low-pass characteristics but to a lesser degree. As a result, besides the broadband driving from impulses affecting all frequencies across B-field, E-field and GIC, low-frequency driving is very efficient in inducing GICs. A further implication for GIC modelling is that periods of low-frequency GIC from low-frequency geomagnetic driving have to be modelled exactly as such and not approximated as dc - including low-frequency driving results in a different system response (Jankee et al., 2020).
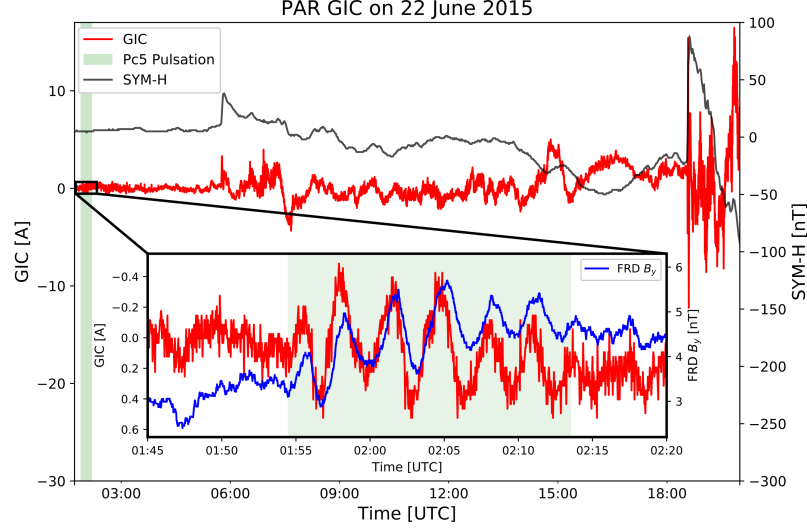
Besides sudden commencements, substorms and other impulsive events, there are secondary drivers which include pulsations (Viljanen et al., 1999; Pulkkinen et al., 2005). At mid-latidues, substorms and their magnetic bay signatures (Watari et al., 2009) do not have the sustained duration to be of concern regarding ac modelling nor the GIC maxima associated with commencements or impulses and are not covered further. Geomagnetic pulsations, i.e. oscillations of the geomagnetic field within the ultra low-frequency (ULF) band (roughly 1 mHz – 1 Hz), are of particular interest though and described in more detail in Section 1.1. These sources tend to be ignored since they are often dwarfed by peak GICs associated with impulsive events. Furthermore, it has been suggested that the rate of change is not extreme enough to cause large GICs (Viljanen et al., 1999). Both these statements are often true, especially at mid-latitudes where the driving current system tends to be the ring current and the auroral and substorm effects are negligible in comparison (de Villiers et al., 2017). In the case of significant low-frequency disturbances, such as pulsations during intense geomagnetic storms, significant GICs could indeed result due to the effective low-pass coupling, which introduces sustained driving. An example of such coupling is seen in recent work in the Kola peninsula which has shown direct links between pulsation-like disturbances and large measured GIC values (Sokolova et al., 2019; Belakhovsky et al., 2019; Kozyreva et al., 2019; Apatenkov et al., 2020). In this paper similar coupling is unexpectedly seen at mid-latitudes, with sustained moderate GICs being produced. The effects on the network of such distinctly low-frequency ac current is the subject of continued research (Jankee et al., 2020), especially when there is exposure over an extended period.

The link between GICs and geomagnetic pulsations has been established in recent literature, although the extent has not always been clear and has generally focused on high-latitudes. During the recovery phase of the 6–7 April 2000 geomagnetic storm, Pc5 pulsations with a period between 5 and 8 minutes were identified in the Finnish power system (Pulkkinen et al., 2003). It was noted that despite the relatively low amplitude of the GIC pulsations (33% of peak at storm sudden commencement), there is a risk of cumulative erosion in pipeline GICs. During the recovery phase of the Halloween Storm, sustained mid-latitude pulsations were noted in the USA (Kappenman, 2005) and in Czech pipelines (Hejda & Bochníček, 2005), which were also identified as Pc5 pulsations. In 10 large storms between 1999 and 2005, there were Pc5 pulsations driving GICs in the local morning or post-midnight sectors at high-latitudes during the recovery phase (Pulkkinen & Kataoka, 2006). A further study similarly looked at the difference in spectra between 32 CME (coronal mass ejection) and 3 CIR (corotating interacting region) driven storms. For CIR storms pulsations in the Pc3–5 range were seen, especially in the local day-side during the recovery phase. Smaller CME storms do not always show pulsations in the recovery phase. In the 27–28 December 2005 CIR storm, low amplitude GIC as a result of pulsations were seen at Memanbetsu, a mid-latitude site in Japan (Watari et al., 2009). More recently, long period pulsations were seen in the high-latitude Kola peninsula during the 28–29 June 2013 geomagnetic storm, producing over 120 A GIC at a particular node in the power grid (Belakhovsky et al., 2019). Pi3-type quasi-pulsations with a period of between 10 and 20 minutes resulted from a sequence of vortex-like localised structures associated with omega-bands (and Ps6 pulsations) (Apatenkov et al., 2020) embedded in a substorm bay that constructively created large GICs (Yagova et al., 2018; Belakhovsky et al., 2019; Apatenkov et al., 2020). Localised long period Pi3 disturbances have also been noted at high-latitudes in the eastward B-field (B_y) component with GIC

risk in north-south effective power networks, contrary to the typical high-latitude east-west GIC driving associated with the large scale east-west auroral electrojet current system (Yagova et al., 2018). Such vortex-like current structures have also previously been related to long period morning Ps6 pulsations, which have shown correlation to particularly large dB/dt and possible GICs (Apatenkov et al., 2004). The link to fine scale disturbances, such as Ps6 pulsations, has been explicitly seen in the Kola peninsula for other events as well, with measured GICs around 25 A (Kozyreva et al., 2019).

At this point it should also be noted that all GIC modelling and analysis depends on the network. There are cases where large geomagnetic disturbances will not be critical to the network, or cases where low amplitude disturbances can be amplified as a result of the network structure and cause damage where not expected. Network effective directionality has a large part to play in modulating the effectiveness of disturbances. When the disturbance has intrinsic directionality that aligns to the network, coupling is maximised. In this paper, only measured GIC data are used and no GIC modelling is done. In some cases, for example the inset of Figure 1, the sign of the measured GIC is inverted to clarify the relation to other parameters since GIC polarity is purely a result the Hall-effect sensor set-up in relation to the structure of the network. For the two measurement sites used in this paper, the sensor set-up is opposite. For the TVA network in the USA, network analysis suggests all nodes take positive GIC as being out of the ground, whereas the Eskom data in South Africa takes positive GIC as into the ground. Both nodes are effectively north-south aligned, with the implication that the north-south E-field would drive GICs. In the TVA network, the majority of the local network lies to the south of the PAR node used, and hence a northward E-field (E_x) will produce GICs that ground and are recorded as negative GICs. In South Africa, the majority of the local network is north of the GRS node used, and a southward E-field ($-E_x$) will produce GICs that ground and are recorded as positive GICs. Empirically, the network parameters scaling the northward E-field to measured GIC in both cases are negative, i.e. $GIC \propto -E_x$. Taking this one step further, in general terms and using the most basic magnetotelluric equation, the northward E-field component E_x is related to orthogonal the eastward component of the B-field B_y though the surface impedance Z, or $E_x = ZB_y$. The E_y and B_x components are similarly related, but out of phase, i.e. $E_y = -ZE_x$ (Cagniard, 1953). Since we are only concerned with a north-south effective power network in this paper, the measured GIC can be loosely related to the B-field as well, $GIC \propto -B_y$, justifying the inverted axis in plots.

Regardless of source, the inductive coupling between dB/dt in the Earth and the geoelectric field that drives the GIC is not linear in the time domain, with the Earth's conductivity needing to be taken into account in the frequency domain. As such, a frequency weighted dB/dt analogous to the geoelectric field is a much better proxy to GICs than simply using dB/dt. Ultimately, it is the geoelectric field that is used in GIC modelling and calculations (Lehtinen & Pirjola, 1985). The geoelectric field and GIC are effectively the output of a low-pass filter of dB/dt at Earth's surface (Oyedokun et al., 2020). Thus, the coupling between B-field variation and the power grid is particularly good at lower frequencies, irrespective of amplitude. Geomagnetic pulsation intervals with periods of 1 minute (in the Pc4 band) and longer are examples of this coupling. In Figure 1, the coupling of Pc5 pulsations to GICs in the frequency domain is apparent, even though both the GIC and B-field amplitudes are very small (dB/dt around 1 nT/min at maximum). At this level of GIC exposure, no damage is expected whatsoever. What is interesting nevertheless is the extent of coupling in the frequency domain, with the low-amplitude low-frequency signal lifted out of the high-frequency noise. Longer period pulsations which often have larger amplitudes and can be effective drivers of sustained and significant GICs. The focus of this paper is on the evidence of significant pulsation driven GICs at mid-latitudes, often not identified or considered, but linking directly to ac modelling of GICs and sustained stress on the power system. Three storms with GIC effective pulsation events are analysed, namely the 2003 Halloween Storm that initiated sig-

Figure 1. Low amplitude 5.3 mHz Pc5 pulsation (green shaded region) in the noise at PAR substation (red) in the TVA network during geomagnetically quiet time (as seen in the SYM-H index). Pc5 pulsations occur in both B-field components, with the H or B_x component contribution often larger. The effective network around PAR extends southwards and mostly the D or B_y component of the nearby FRD magnetic observatory B-field (blue) is apparent in GIC data.

nificant accumulated damage in the South African power network and was the largest geomagnetic storm in solar cycle 23; an apparently typical intense geomagnetic storm in June 2015 and finally the famous March 1989 Storm that led to the collapse of the Hydro-Québec power network and is now used for regulatory benchmarking (*TPL-007-1: Transmission System Planned Performance for Geomagnetic Disturbance Events*, North American Reliability Corp., 2017.). The first two storms make use of measured GIC data, whereas the last storm is the widely used benchmark geomagnetic disturbance (GMD) event for power utilities which uses derived E-field data. The benchmark event is included specifically to show that low-frequency GIC modelling of the network response is needed given the existence of GIC effective pulsations. It is further shown that using a proxy with incorrect frequency weighting such as dB/dt may not reproduce the effects of pulsations at frequencies significantly lower than the sampling frequency.

1.1 Geomagnetic pulsations

Pulsations of Earth's B-field, also called geomagnetic fluctuations or oscillations, have been been studied since the 1800's. As research in the field grew, a classification system developed to group similar pulsations by source, period and other general characteristics. In broad terms there are continuous pulsations (Pc1–6) which are truly periodic and sinusoidal and irregular pulsations (Pi1–3) which are quasi-periodic and often sit on magnetic bays (Saito, 1969). Within these broad pulsation classes there are further subclasses, particularly within the irregular pulsation classes. In this paper long period pulsations in GIC data are linked to geomagnetic pulsations, specifically in the Pc5 (periods of a few minutes) and Ps6 (subclass of Pi3 pulsations, with periods of tens of minutes) bands of ULF.

Pc5 pulsations (period 150 – 600 s) are 'continuous' type pulsations with durations of tens of minutes and commonly seen in the auroral oval. Various generating mechanisms exist, from global magnetospheric oscillations to more small-scale, localised sources.

Shear waves due to Kelvin-Helmholtz type oscillations of the magnetospheric boundary layers, driven by high speed solar wind can cause global modes of oscillation; pressure fluctuations in the solar wind can cause a rippling of the magnetopause, propagating waves to the inner magnetosphere where coupling to local field line resonance modes cause the surface magnetic field to fluctuate at Pc5 frequencies (Walker, 2005). Stephenson and Walker (2002) presented evidence of Pc5 band waves in the solar wind entering the magnetosphere and coupling directly to field line resonances at the appropriate L-shell. Storm time Pc5 waves generally have high amplitudes (up to order of magnitude higher than quiet time Pc5's) and global coverage. It is these type of extreme event Pc5 pulsations that are seen at mid-latitudes, which otherwise would be constrained to Pc3 pulsations given only field line resonances. Pilipenko et al. (2010) provides a good overview of global large amplitude Pc5 pulsations and showed that they mostly occur during storm recovery phase, driven by high speed solar wind streams in the presence of increased solar wind pressure. The high speed stream sets up a Kelvin-Helmholtz instability, causing magnetohydrodynamic oscillations in the global magnetospheric waveguide. During intense storms significant wave power can penetrate to low-latitude regions (Pilipenko et al., 2010). The Pc5 pulsations are not the result of near-Earth current systems that typically disturb the B-field and drive GICs, but rather the global ringing of the B-field itself. Both horizontal B-field components are affected, but the H or B_x component (i.e. the geomagnetic or geographic north component, roughly aligned to the Earth's main field) is usually larger. In this paper focus is placed on the horizontal B-field components as we are specifically interested in GIC linked disturbances. The horizontal B-field field components are thought to be GIC effective as they have the largest contributions to inducing the horizontal E-field which drives GICs. For these horizontal Pc5 B-field pulsations global power systems are affected, with both north-south and east-west effective nodes being susceptible. East-west nodes are however more affected due to the larger H component contribution inducing a larger roughly orthogonal geoelectric field.

Periods longer than Pc5 can be classified either in the general Pc6 or Pi3 bands. Pc6 pulsations are an entirely different form of continuous pulsations as their period is too long for any cavity mode in the magnetosphere. These pulsations are more associated with tail dynamics or fluttering. There would also be cases where periodic substorms show apparent periodicity by chance. A better defined class of pulsations that overlap with Pc6 pulsations are Ps6 pulsations. These Ps6 pulsations are long period irregular pulsations in the Pi3 band associated with substorms and with periods ranging from 5 to 40 minutes, mostly seen in the D (or B_y) component of the B-field and originally defined in the auroral zone (Saito, 1978). Ps6 events are thought to be driven by the fluctuation and 'meandering' of the ground-based footprints of field-aligned current systems observed during substorms. They usually occur in conjunction with so-called omega-band auroral structures at the equatorward boundary of the aurora (Saito, 1978; Lühr & Schlegel, 1994; Amm et al., 2005) during substorm onset (Wild et al., 2011) or recovery (Saito, 1978) phases. These ionospheric manifestations of omega-bands and Ps6 pulsations are further thought to be the end of a chain of processes starting with Earth directed flow bursts in the magnetotail (Henderson et al., 2002). Compared to the global Pc5 events, Ps6 events are distinctly different, being more localised and affecting north-south nodes in a power network due to the dominant D component of the B-field. The spatial localisation of these pulsations applies both in latitude and longitude, with longitude drift between 0.4 and 2 km/s often seen in auroral regions. Large power grids can span large areas and as such these meandering structures can move across different sections of a network, making dense B-field measurements necessary.

2 Data and Processing

Three pulsation events are selected from intense geomagnetic storms, defined as geomagnetic storms when the *Dst* (or higher resolution SYM-H) minimum is less than

Table 1. Stations and data used in analysis of GIC effective pulsation events. Geomagnetic co-ordinates are given as at date and using a quasi-dipole approximation.

Event	Date	Type	Station (Abbr.)	Data	Geog. Lat.	Geog. Lon.	Geom. MLat.	Geom. MLon.	Cadence
1	31/10/2003	Pc4 Pc5	Grassridge (**GRS**)	GIC	-33.7°	25.6°	-42.3°	90.1°	2 s
			Hermanus (**HER**)	$B_{x,y}$	-34.4°	19.2°	-42.6°	83.3°	60 s
2	23/06/2015	Ps6	Paradise (**PAR**)	GIC	37.3°	-87.0°	47.4°	-13.8°	2 s
			St John's (**STJ**)	$B_{x,y}$	47.6°	-52.7°	51.6°	31.5°	1 s
			Ottawa (**OTT**)	$B_{x,y}$	45.4°	-75.6°	54.6°	2.9°	1 s
			Fredericksburg (**FRD**)	$B_{x,y}$	38.2°	-77.4°	47.8°	-0.2°	1 s
			RES46 (**RES**)	$B_{x,y}$	37.5°	-87.6°	47.6°	-14.6°	1 s
			TNV47 (**TNV**)	$B_{x,y}$	35.4°	-87.5°	45.6°	-14.5°	1 s
			Stennis Space Center (**BSL**)	$B_{x,y}$	30.4°	-89.6°	40.5°	-17.5°	1 s
			Port Stanley (**PST**)	$B_{x,y}$	-51.7°	-57.9°	-39.2°	10.9°	60 s
			King Edward Point (**KEP**)	$B_{x,y}$	-54.3°	-36.5°	-45.3°	25.7°	60 s
			Orcadas (**ORC**)	$B_{x,y}$	-60.7°	-44.7°	-48.7°	20.4°	60 s
			Argentine Islands (**AIA**)	$B_{x,y}$	-65.3°	-64.3°	-50.9°	9.6°	60 s
3	15/03/1989	Pc5	Ottawa (**OTT**)	$B_{x,y}$	45.4°	-75.6°	56.7°	0.0°	10 s

-100 nT (Gonzalez et al., 1994). Table 1 summarises the events, locations and the types of data used.

For Events 1 and 2, or the 2003 Halloween Storm and June 2015 storm respectively, there is measured mid-latitude GIC data in which significant pulsation driving is evident. Event 1 makes use of GIC data from the Eskom network in South Africa and Event 2 uses data from the Tennessee Valley Authority (TVA) network in the USA. These events also make use of a range of INTERMAGNET (`www.intermagnet.org`) B-field measurements at the best cadence available in each case. The June 2015 storm also overlaps with local raw B-field data from the USArray Transportable Array sites RES46 and TNV47 (`http://dx.doi.org/10.7914/SN/EM`) which are used for drift estimation.

In Event 3, which is the Hydro-Québec March 1989 Storm, the induced geoelectric field is derived from B-field measurements (B_x and B_y) and used as proxy for GIC

as no utility data was available for this event. The B-field and hence E-field field associated with Event 3 is the 10 second cadence benchmark profile used to inform utility GIC modelling, as defined by the North American Electric Reliability Corporation (NERC) (*TPL-007-1: Transmission System Planned Performance for Geomagnetic Disturbance Events*, North American Reliability Corp., 2017.). The B-field was measured at NRCan's Ottawa (OTT) geomagnetic observatory and the generally well used and understood resistive Québec Earth model was used to the derive the benchmark geoelectric field (Boteler, 2015). The layered-earth model used has layer thicknesses (from top to bottom) of $[15, 10, 125, 200]$ km, with corresponding resistivities of $[20000, 200, 1000, 100]$ Ωm and a half-space resistivity of 3 Ωm. The resistivities in turn define a 1D surface impedance Z that relates the B and E-fields in the frequency domain.

To ensure that periods exhibiting pulsation characteristics in GIC (or geoelectric) data are in fact associated with geomagnetic pulsations, there have to be similar characteristics in the B-field data, i.e. period and duration. Common characteristics would rule out network or resonance effects that would only be seen in the GIC data. GIC (or E-field) data are compared with B-field measurements in the frequency domain to ensure that oscillations of the same period are seen at the same time in both signals and are coherent. The sampling cadence is fine enough and disturbances long enough that the well defined and finite pulsation signatures are not a product of measurement noise or chance.

During the three selected geomagnetic storms, various processes result in different signatures in the horizontal B-field. The superposition of these signatures complicates the detection of pulsation waveforms. Pulsation signature detection is done by taking a rolling FFT of each signal and pre-whitening. Pre-whitening is done by normalising the spectrum according to frequency dependant baseline noise, found by fitting a linear trend in log-space of the power spectrum. To ensure the resulting spectral peaks are significant, significance levels of 5 sigma above the mean power are required for all signals (B-field and GIC/E-field) concurrently. In short, this is a band-agnostic pulsation detection process that does not rely on passing only a specific band of interest.

3 Analysis of GIC Effective Pulsation Events

Modern GIC risk analysis to utilities has focused largely on peak GIC values and the associated thermal damage to transformers, with a lesser emphasis on control system disruptions and harmonic production. Recently such risk analysis has been formalised with NERC, in compliance with a FERC ruling regarding the development of a geomagnetic disturbance reliability standard for utilities (*Federal Energy Regulatory Commission: Reliability Standard for Transmission System Planned Performance for Geomagnetic Disturbance Events. Order 830*, Sep 2016, Washington DC.), developing a reliability standard for utilities regarding GMD risks (*TPL-007-1: Transmission System Planned Performance for Geomagnetic Disturbance Events*, North American Reliability Corp., 2017.). This reliability standard focusses on peak GIC amplitudes and thermal damage with a risk limit of 225 A in the neutral, but does not include sustained driving at lower amplitudes such as is seen during pulsation intervals. The fact that the sustained driving continues for an extended period may be significant in an accumulative damage or voltage stability sense. Such accumulated degradation may be at the heart of transformer failures in New Zealand and South Africa where the GICs in the neutral were likely not more than 19.5 and 45 A respectively, i.e. not particularly large (Divett et al., 2018; Moodley & Gaunt, 2017). Saturation for a 'resilient' three-phase three-limb transformer can occur with currents as low as 6 A (Gaunt & Coetzee, 2007), creating localised hotspots and bubbles in the transformer paper/oil and partial discharge (Khawaja & Blackburn, 2009) that can initiate further degradation (or accelerate existing degradation) under normal operation. The expectation is that even more damage will occur during sustained elevated driving from pulsations. Once degradation has occurred, even with oil changes,

312 there is no reversal possible of the damaged insulation and the transformer has increas-
313 ingly less resistance to future damage (Khawaja & Blackburn, 2009; Moodley & Gaunt,
314 2017). From that point on, the transformer is ultimately on a trajectory to premature
315 failure. Zooming out from the transformer level, voltage stability and protection mal-
316 operation under sustained quasi-dc or rather low-frequency driving can create further
317 complications and points of failure in the power system. The extent of unbalance and
318 distortion introduced by low-frequency GIC instead of dc GIC is the subject of contin-
319 uing research (Jankee et al., 2020). Taking the accumulated damage viewpoint, GIC ef-
320 fective pulsations can be defined as events with peak-to-peak magnitudes of 6 A or higher
321 and/or an extended duration of multiple cycles over a period of minutes.

3.1 Event 1: 2003 Halloween Storm

323 During the well known Halloween Storm of 2003, the biggest of solar cycle 23, con-
324 secutive CMEs resulted in a superstorm with known damage to power grids at mid-latitudes
325 (Gaunt & Coetzee, 2007). High-latitude networks also experienced faults, e.g. a low-set
326 overcurrent relay in Malmö experienced tripping as a result of harmonics during the main
327 phase of the storm on 30 October (Pulkkinen et al., 2005).

328 On 29 October, during the main phase of the first storm, GIC data showed pul-
329 sations due to Kelvin-Helmholtz shearing at mid-latitudes in the North American power
330 grid (Kappenman, 2005) and in Czech pipelines (Hejda & Bochníček, 2005). During the
331 storm recovery phase on 31 October, more Pc5 pulsations were seen in the mid-latitude
332 Czech pipelines. According to Sakurai and Tonegawa (2005) these Pc5 pulsations were
333 some of the largest ever recorded in the Pc5 band.

334 The global pulsations identified in the recovery phases of the consecutive storms
335 were found to have more complicated drivers than typical pulsations, with the disturbed
336 solar wind having a large effect (Pilipenko et al., 2010; Marin et al., 2014). These global,
337 storm time, intense Pc5 events can be seen at fairly low-latitudes and in particular in
338 the morning and evening flanks (Pilipenko et al., 2010). At mid-latitudes all local time
339 sectors were affected, with the largest disturbances of up to 150 nT seen in the pre-noon
340 or noon sectors (Potapov et al., 2006). The solar wind driven pulsation periods were also
341 confirmed in satellite data, with further analysis of Pc3 pulsation transition at the plas-
342 masphere boundary (Balasis et al., 2015). During the periods of 05:37 to 07:40 UT and
343 11:00 to 14:00 UT on 31 October, large amplitude Pc5 pulsations were identified in An-
344 denes (high-latitude station in Norway) and Iriomote (low-latitude station in Japan) (Sakurai
345 & Tonegawa, 2005).

346 In South Africa, at the GRS substation, GIC data shows the intense Pc5 pulsation
347 activity from 05:37 to 07:40 and 11:00 to 14:00 UT (partially shown in the shaded re-
348 gions of Figure 2); these are the same extreme pulsations periods discussed by Sakurai
349 and Tonegawa (2005). During the 2 to 3 hours of pulsation driving, amplitudes of up to
350 65% of the peak GIC measured near storm sudden commencement (SSC) were seen. GRS,
351 where the GIC measurements were made, is a north-south effective node and driven mainly
352 by the weaker B_y component of the Pc5 pulsation. Of the two Pc5 pulsation intervals
353 shown, the first between 05:37 and 06:40 has a slightly longer period of around 295 s com-
354 pared to the second between 11:00 and 12:00 with a period of around 255 s. This first
355 interval shows larger amplitude B-field oscillations and GICs. Given an east-west node,
356 which is driven by the stronger B_x component, the associated geoelectric field would be
357 larger. This possibly occurred at the Matimba power station in the north of South Africa
358 where significant accumulated damage of transformer insulation was recorded as a re-
359 sult of the Halloween Storm (Gaunt & Coetzee, 2007). Further analysis of magnetome-
360 ter data between 04:30 and 09:30 at the Hartebeeshoek and Tsumeb INTERMAGNET
361 stations, in the north of South Africa and Namibia respectively, show comparable or marginally
362 larger B-field pulsation amplitudes at the low-latitude stations compared to HER, i.e.
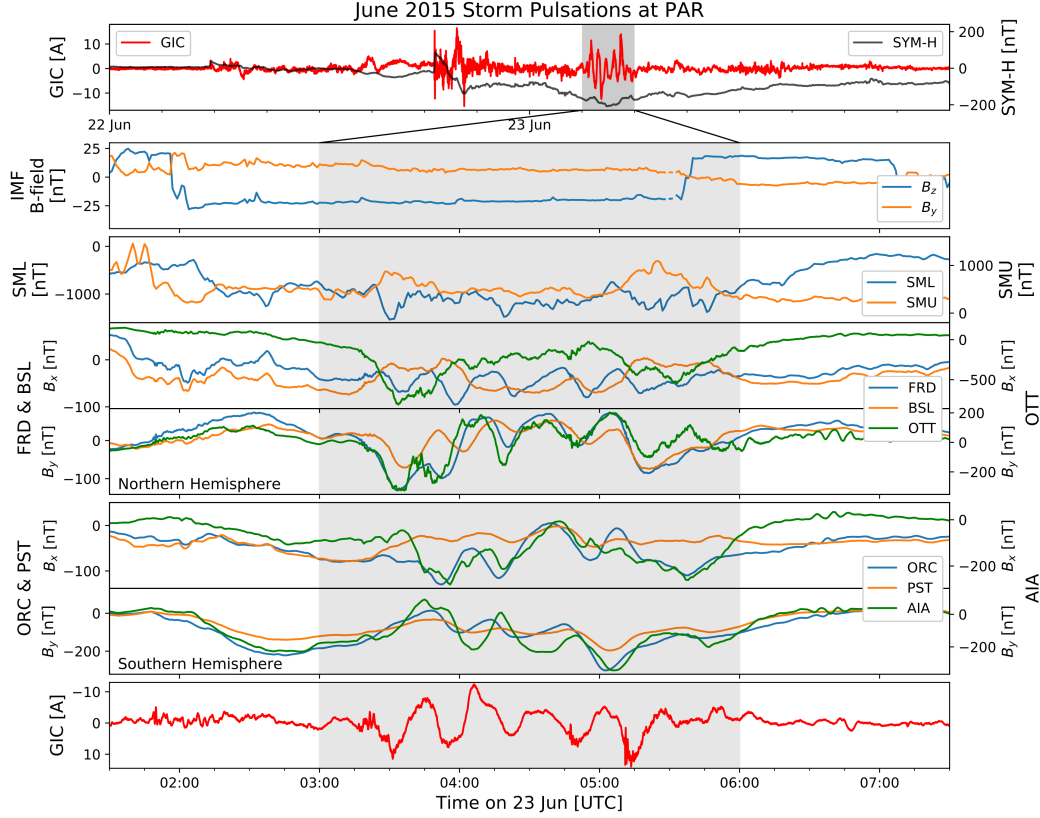
Figure 2. Various pulsations seen in GRS GIC data (red) during recovery phase of the 2003 Halloween Storm. Also shown is the B_y component at HER (blue), which would link to a north-south effective grid such as at GRS. Left subfigure shows Pc4 pulsations not resolved by 1 minute B-field data. Middle and right subfigures are part of previously defined periods of extreme amplitude global Pc5 pulsations (Sakurai & Tonegawa, 2005).

the global Pc5 pulsations penetrated to around -30° geomagnetic latitude in the Southern Hemisphere without a loss of power. This diverges from the typical view of Pc5 amplitudes decreasing with latitude (Saito, 1969) and the extent of penetration of global Pc5 pulsations seen in the Northern Hemisphere for the same event (Pilipenko et al., 2010). Across all stations, the pulsations in the B_x component were larger than the B_y component.

Also of interest are the localised Pc4 pulsations embedded on a magnetic bay (and hence multiplying their effect) with periods just short of 2 minutes unresolved in magnetic field data but seen in GRS GIC data between 00:15 and 00:45 UT (also shown in Figure 2). The Pc4 pulsations aren't seen in the B-field due to 1 minute B-field sampling with a Nyquist frequency of 8.3 mHz not fulfilling the Nyquist criterion for 8.8 mHz pulsations. Data from local induction pulsation magnetometers at HER and Sutherland (-32.38°, 20.81°), operated by the South African National Space Agency, confirm the presence of these Pc4 pulsations in the B-field at 1 s cadence.

3.2 Event 2: June 2015 Storm

On 22 June 2015, the arrival of a CME triggered an intense, but not extreme, geomagnetic storm (SSC at 18:33 UT) with minimum SYM-H of -208 nT reached around 04:30 UT (see Figure 3). In contrast to the relatively rare Halloween superstorm, this storm can be classified as just within the threshold of a great geomagnetic storm ($Dst \leq$ 200 nT) (Le et al., 2012). Taking into account six solar cycles (1957-2018), there are on average roughly 13 such great geomagnetic storms per 11 year cycle. During this particular event, significant GIC was recorded at the PAR substation in the Tennessee Valley Authority (TVA) network, south-eastern USA. A peak absolute value of 16.46 A was reached within two hours after the SSC and further oscillations with peaks between 7 and 14 A (peak-to-peak variations of between 14 and 28 A) occurred near the minimum of the storm. Storm minimum occurred pre-midnight (22:43 MLT) in the TVA network
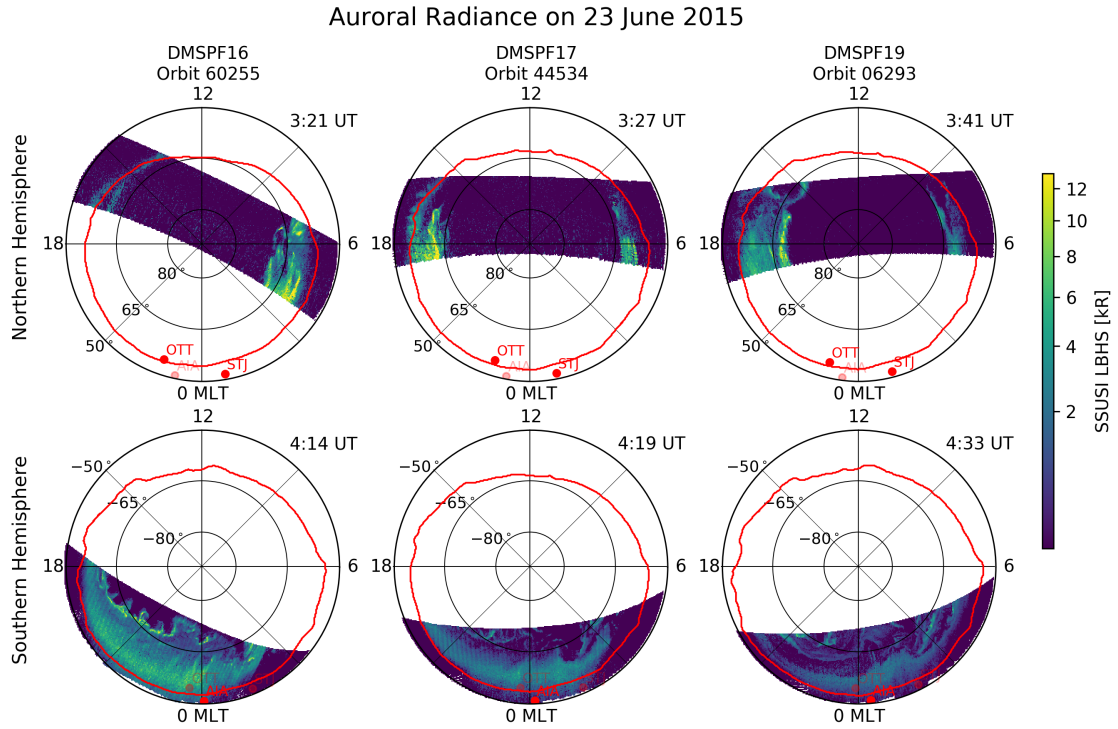
Figure 3. 23 minute period Ps6-type disturbance as measured in GIC data at PAR in the TVA network between 03:30 and 05:30 UT (bottom panel), coinciding with the peak of the main phase of the geomagnetic storm (top panel). Also shown are IMF B_z and B_y components, the SuperMag SML and SMU electrojet indices (Newell & Gjerloev, 2011) and B_y component at nearby stations and congruent stations in the Southern Hemisphere.

389 and was bookended by two major substorms with expansion phases at about 03:16 and
390 05:09 UT (Nakamura et al., 2016). It is during the time between the two substorms that
391 high amplitude oscillations with period of around 23 minutes are observed in the B-field
392 across eastern North America and in the PAR GIC data shown here. Particle precipi-
393 tation and currents associated with these substorms resulted in a strong westward elec-
394 trojet (seen in the SML index (Newell & Gjerloev, 2011) in Figure 3), field-aligned cur-
395 rents of around 6–7 MA (Nakamura et al., 2016) and equatorward travelling ionospheric
396 disturbances (Ngwira et al., 2019). As the storm was reaching its peak, the equatorward
397 edge of the auroral oval as estimated by the SSUSI measurements (Paxton et al., 1992,
398 1993, 2017) was around 53° geomagnetic latitude and centred around the longitudinal
399 region of interest (see Figure 4).

400 Regular long period oscillations in the B-field field over widespread regions in the
401 midnight sector are reminiscent of the Ps6 disturbances that usually occur in conjunc-
402 tion with omega-band auroral structures (Saito, 1978; Lühr & Schlegel, 1994; Amm et
403 al., 2005; Apatenkov et al., 2020) near substorm onset (Wild et al., 2011; Connors et al.,
404 2003) or recovery (Saito, 1978; Amm et al., 2005) phases. Some authors prefer the term
405 disturbance because these are not pulsations in the sense that they are the direct ground-
406 based observations of magnetohydrodynamic wave activity (Connors et al., 2003). The
407 ground-based low-frequency (4–40 minute period) Ps6 fluctuations in B-field are under-

stood to be signatures of meandering field-aligned current systems on the ground (Lühr & Schlegel, 1994; Amm et al., 2005). Congruency between hemispheres is expected, although slight asymmetry may be seen due to the small but non-zero IMF B_y component. The congruency is seen in Figure 3, which focuses on the ground B-field footprint of the Ps6 pulsations. Similar to most other figures in this paper, the top panel of Figure 3 shows large scale profile of the geomagnetic storm in the SYM-H component and the associated GIC time series. In the second panel, the changes in the IMF that triggered the substorms – seen in the SML and SMU indices (third panel) – are shown. The fourth and fifth panels show magnetic field at magnetic observatories around PAR substation: OTT to the far northeast of PAR, FRD (east) and BSL (south). Fluctuations in B-field are seen at 23 minute period at all these stations, especially in the D or B_y components (which is characteristic of Ps6 (Connors et al., 2003)), in phase with the GIC oscillations at PAR (bottom panel). In the sixth and seventh panels, Southern Hemisphere stations show similar B_y pulsation signatures, but in this case out-of-phase with their Northern Hemisphere counterparts as expected (Connors et al., 2003). The congruency between hemispheres allows probing of the auroral structure as seen from the SSUSI instrument aboard the sun-synchronous DMSP satellites. For this event, there was good coverage of the Southern Hemisphere as seen in Figure 4. Specifically of interest is the southern section of the F16 and F17 orbits, where an auroral bulge is seen along with auroral streamers and omega-bands. For reference AIA, ORC and PST sit at around 00:04, 00:48 and 00:10 MLT respectively. For the same orbit sections OTT, FRD and BSL sit around 23:38, 23:25 and 22:16 MLT respectively.

In the case of a pre-midnight substorm, it has been suggested that Ps6 disturbances would be associated with the westward electrojet resulting from a substorm current wedge and exhibiting westward or sunward drift (Saito, 1978). Similarities in the structure of intensifications in the westward electrojet SML index support this link. Making use of B-field data from the EarthScope USArray magnetotelluric sites RES46 and TNV47 (`http://dx.doi.org/10.7914/SN/EM`) that coincided with this event, it is evident that there is westward drift. Site RES46, which is at almost exactly the same geomagnetic latitude as FRD shows a statistically significant westward drift. Propagated to an auroral region of 66° MLon (assuming a spherical Earth) and converting to an eastward drifting reference frame where previous omega band drift estimates were made, the average drift speed (95% confidence interval) is is roughly 1.89±0.35 km/s (0.04° MLon/s), although exact drift speeds between peaks differ. This general westward drift is consistent with drift between other sites not on exactly the same magnetic latitude. Looking at a north-south chain of either OTT and FRD, or RES46 and TNV47, there is no statistically significant lag nor change in period of pulsations, i.e. that is no latitudinal drift and it not expected that the disturbances arise from field lines but rather current systems. This drift of current systems means there is fine spatial scale movement of the localised pulsation footprint, and in turn localised measurements are needed for GIC modelling given a Ps6 event even though B-field disturbances at mid-latitudes are often assumed to be nearly homogeneous over large areas for practical purposes (Ngwira et al., 2009). The Ps6 signal at OTT suggests a mix of clockwise and anti-clockwise polarisation, which is typical of central pre-midnight Ps6 disturbances in auroral regions (Saito, 1978). OTT in this case is within the aurora, which is consistent. The Ps6 disturbance occurs during a period of strong southward interplanetary magnetic field (IMF) buffeting ($B_Z \approx -20$nT for about 3 hours) which enabled the anti-earthward stretching of the magnetotail, right before a sudden dipolarisation or reconnection of the tail due to abrupt northward turning of B_Z (Reiff et al., 2016). When the magnetotail snaps back to Earth, the Earthward fast flow may drive Ps6 type disturbances (Cheng et al., 2014; Henderson et al., 2002). It is possible that the first substorm injection and tail dynamics may have initiated the Ps6 disturbances and the second injection turned off the driving Kelvin-Helmholtz instabilities that were initially created.
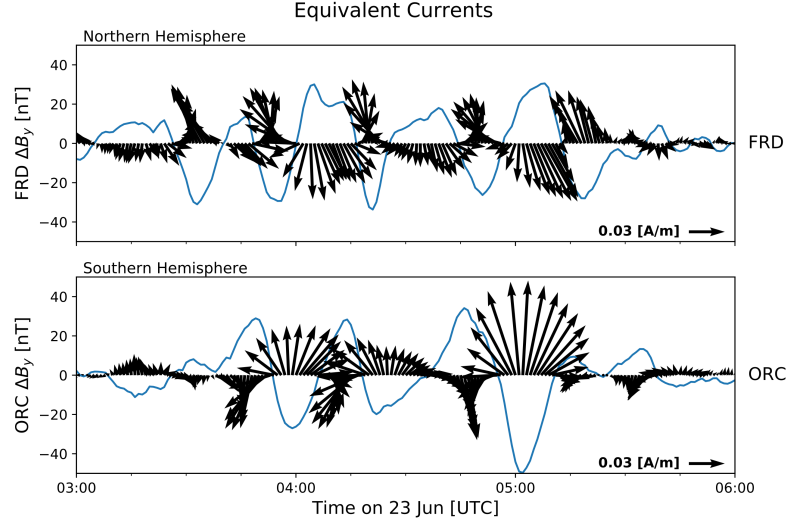
Figure 4. Auroral radiance in the LBH Short band from the SSUSI instrument aboard the DMSP satellites during Event 2 https://ssusi.jhuapl.edu/. The equatorward boundary of the aurora as determined by the GUVI model is shown in red. The passes over Southern Hemisphere in this case include the longitudinal regions of interest.

Although Ps6 events are well known and have also recently been seen in GIC data elsewhere (Kozyreva et al., 2019; Apatenkov et al., 2020), it has largely been thought that they are restricted to high-latitudes. Why this average storm in particular is so effective at mid-latitudes is still an open question. It is most likely that multiple factors work together. Strong electric fields are seen to add to the Ps6 driving (Connors et al., 2003), along with increased ionospheric conductivity seen during the summer solstice (June in the Northern Hemisphere as observed) (Rostoker & Barichello, 1980). The equatorward expansion of the auroral oval at the peak of a geomagnetic storm allows particle precipitation at lower latitudes. The substorm field-aligned currents observed (6–7 MA) (Nakamura et al., 2016) are also significantly stronger than for typical omega-bands associated with Ps6 events (2 MA). The more typical Ps6 event observed in GIC data in the Kola peninsula, which produced GICs of 25 A, also has a significantly shorter period (Kozyreva et al., 2019). Perhaps more likely is that the observed mid-latitude disturbances are a manifestation of the field aligned currents (FACs) associated with omega-band structures in the auroral region. Apatenkov et al. (2020) recently presented a rigorous study of the omega-band driving of the extreme Pi3/Ps6 disturbances in the Kola peninsula which produced the largest GICs seen in that region. This is the same event which had previously been associated with localised current vortices (Belakhovsky et al., 2019). These current vortices are FACs that are associated with omega-bands, each omega-band having a pair of upward and downward FACs (Amm et al., 2005; Wild et al., 2000; Lühr & Schlegel, 1994). Using the approach of equivalent current vectors from the B-field, we can get an idea of the FAC structure associated with omega-band vortices (Lühr & Schlegel, 1994; Wild et al., 2000). Assuming an E-region sheet current greater in extent than the height of the E-region, then directly above the magnetometer we have the equivalent current components $J_{x,y}$ given by,

$$J_x = -\frac{2}{\mu_0}\Delta B_y \quad \text{and} \quad J_y = \frac{2}{\mu_0}\Delta B_x, \tag{1}$$

where $J_{x,y}$ is in Am, $\Delta B_{x,y}$ is the disturbance field in nT and μ_0 is $4\pi\times10^2$ nTm/A. The disturbance B-field is estimated through a first-order high-pass Butterworth filter with a cut-off period of 30 minutes to include all variation from the pulsation. The equivalent current vectors are shown for FRD and ORC, which are at a similar geomagnetic latitude in the northern and southern hemispheres, in Figure 5. Firstly, since the Ps6 pulsations have a westward drift from magnetometer readings, the axes does not have to inverted for spatial consistency. Any time offsets due to longitudinal separation are also ignored since only a qualitative idea of the localised FAC structure is needed. For each omega-band, a downward FAC with its clockwise Hall current is paired with an upward FAC with an anti-clockwise Hall current. Looking at the FRD current vectors, it is evident that they rotate in an anti-clockwise direction. For a westward drifting system this suggests FAC pairs are poleward of FRD. Not shown, but similar is the response at OTT, where the current vectors are stronger and not quite as clearly defined with a mix of clockwise and anti-clockwise directions. OTT is under the aurora during this event and with a near proximity to the still further poleward FACs, the response is expected. For ORC in the Southern Hemisphere, the vectors rotate in a clockwise direction, also suggesting a poleward current system. Given that pairs of FACs form the omega-bands, the number of bands in the pulsation train can be determined. Between FAC current pairs there are either strong poleward or equatorward equivalent currents, depending of the order of the pair. Shorter poleward intensifications at FRD should be associated with the region between an upward FAC on the western front and downward FAC on the eastern front. Longer equatorward intensifications would have the opposite orientation with an upward FAC on the eastern front and downward FAC on the western front for westward drifting structures. In the opposite hemisphere, ORC will have similar effects but with the poleward and equatorward intensifications reversed. In both hemispheres, and upward FAC precedes a downward FAC as the system drifts westward over the magnetometers. From this five omega bands pass over the FRD longitude sector and four pass
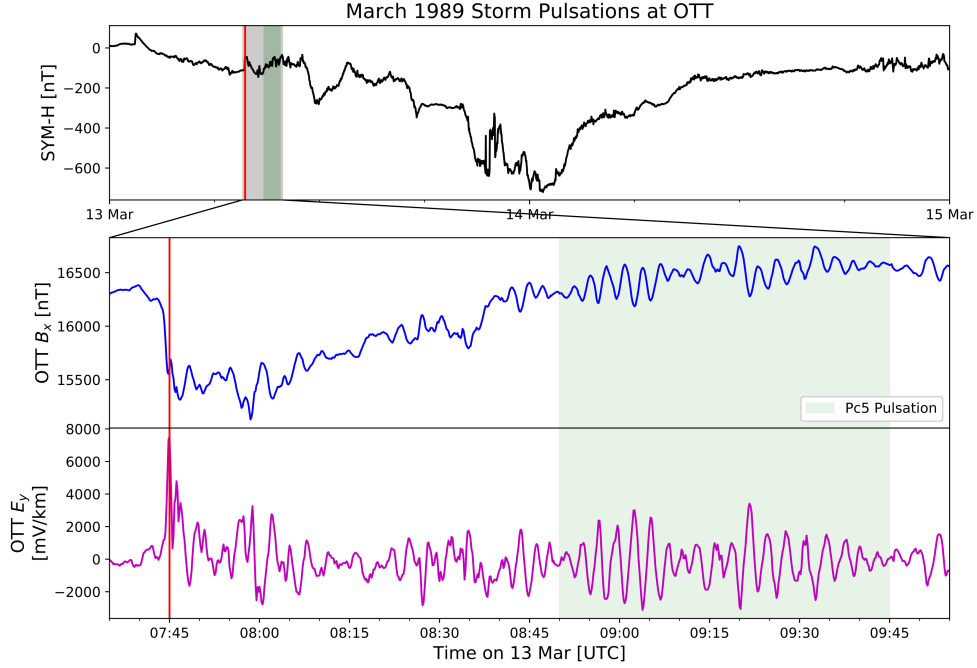
Figure 5. Equivalent current vectors along with the disturbance B-field ΔB_y component for FRD and ORC, both at similar latitudes but in opposite hemispheres.

over the ORC longitude sector. The drift and order of FAC pairs in this pre-midnight Ps6 event is opposite of what is typically seen in post-midnight sector events. Ultimately the Ps6-type mid-latitude pulsations are effects of strong auroral FACs. Regardless, such low-frequency driving couples exceedingly well to GICs (discussed further in following section) and can arise from seemingly average geomagnetic storms.

As mentioned previously, such regular, long period, high amplitude oscillations in GIC driving can cause significant accumulated damage or ageing to equipment – possibly more so than typical higher frequency pulsations. Comparing the roughly two hour period of Ps6 activity to a similar duration of activity after the SSC, which included the most active part of the main phase, the RMS of the GIC (in Amperes) during Ps6 driving exceeded that of the SSC and main phase onset by 10%. The Ps6 activity is furthermore cyclical, with sustained and constant repeated GIC driving that possibly stresses transformers more. The nature of the power system response given such driving is part of ongoing research.

Even though the Ps6 event was seen in measured GIC data in the entire TVA network, it has a predominant direction. Specifically, the dominant D component of the B-field drives a stronger north-south geoelectric field that affects north-south nodes such as PAR more. TVA was not the only network affected – at a substation in a neighbouring network the GIC pulsation peaks were around 25 A. The extent of the geomagnetic disturbance – about 15 degrees in geographic latitude and 30 degrees geographic longitude – means that the entire eastern North America was likely affected, modulated by local ground conductivity conditions. A possible mitigating factor is that such an event will always occur in the local night time or morning sector (Viljanen et al., 2001). At the same time however the pulsations are likely to be part of a geomagnetic storm and occur after the system has already been stressed by the sudden storm impulse and main phase driving, i.e. the largest sustained cumulative stressing comes after the system is already stressed and vulnerable. It is most unlikely that gas bubbles formed in transformer winding insulation during the initial onset of the storm would be reabsorbed by the time of the pulsation activity. During the second stronger period of accumulated driving, further partial discharge could increase ageing and accumulated damage.

Figure 6. Time series of the detected Pc5 pulsations (green shaded region) at OTT during March 1989 storm using the NERC defined benchmark geoelectric field (magenta) (*TPL-007-1: Transmission System Planned Performance for Geomagnetic Disturbance Events*, North American Reliability Corp., 2017.). A red line indicates the time of collapse of the Hydro-Québec network (Boteler, 2019).

3.3 Event 3: March 1989 Geomagnetic Storm

Event 3 is included in this analysis specifically because it plays such a critical role in current utility and modelling benchmarking. The March 1989 geomagnetic storm that resulted in the now famous Hydro-Québec blackout (Bolduc, 2002; Boteler, 2019) can probably be regarded as the catalyst for the intense modern study of GICs. In the NERC reliability standard, this storm, along with its B-field and derived E-field profiles at OTT, is used as the regulatory benchmark for utility planning. As stated above, only peak GIC hence driving E-field values are considered in the standard. Nevertheless, embedded in the geomagnetic and geoelectric profiles for OTT there are 6 mHz Pc5 pulsations with significant amplitude for about an hour around 09:00 UTC, as seen in Figure 6. Given that these pulsations are already in the NERC benchmark GMD profile, modelling should ultimately aim to analyse the effects of such low-frequency GIC driving in a power system context.

Although OTT is a high mid-latitude station where Pc5 pulsations are likely to occur, pulsations were also seen at lower mid-latitudes in Europe (Villante et al., 1990) suggesting the type of global Pc5 event seen during geomagnetically disturbed periods (Pilipenko et al., 2010). Pc5 pulsations are more often associated with the H component of the B-field, and as such the variation would affect the east-west geoelectric field component and east-west networks more. In the case of the Hydro-Québec blackout, it is likely that the second of a series of CMEs coincided with a substorm which resulted in a large eastward electrojet that knocked out the power system (Boteler, 2019). For the NERC benchmark event these pulsations at OTT result in an oscillating east-west geoelectric field of roughly
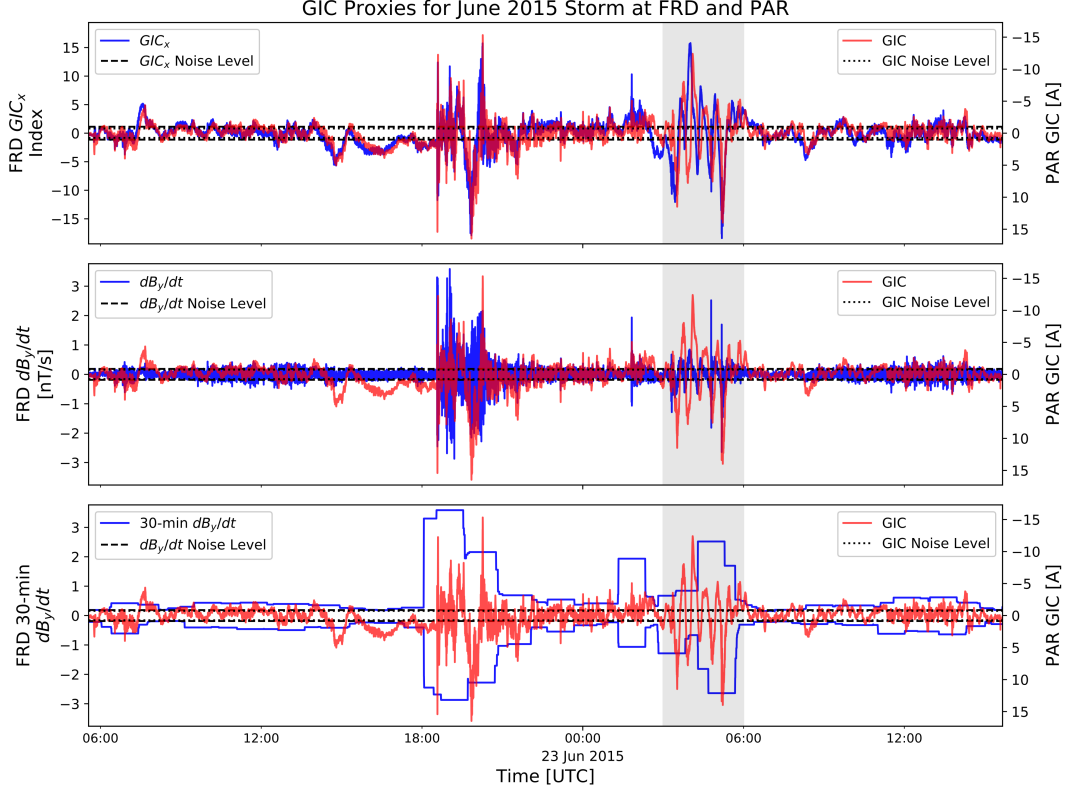
2 V/km (4 V/km peak-to-peak) over a sustained period (Figure 6). This geoelectric field level is 25% of the 8 V/km extreme case for thermal damage (*TPL-007-1: Transmission System Planned Performance for Geomagnetic Disturbance Events*, North American Reliability Corp., 2017.) but may result in significant accumulated damage and control maloperation. The exact nature of such damage due to pulsations in Event 3 is not known since the Hydro-Québec outage happened during the shock impulse at 07h45 (Boteler, 2019), before either the Pc5 pulsations or the peak of the storm. As alluded to above, if the network had not collapsed but rather been in a stressed state, the pulsation driving may even more effective at introducing damage. The fact the pulsations occurred before the main phase of the superstorm is of interest when compared to the similar Pc5 pulsations in the recovery phase of the 2003 Halloween storm. In the case of the 1989 storm, the Pc5 pulsation period followed the SSC of a high-speed CME, which in turn followed an initial CME that had already disturbed the near-Earth environment (evidenced by the SSC coinciding with a substorm), possibly having similar effects to the 2003 Halloween storm. Multiple CME scenarios are inherently more complex, with subsequent CMEs having faster speeds after their path is cleared by a preceding CME (Boteler, 2019), and possibly triggering intense substorms (Tsurutani et al., 2015). Besides being more complex, these multiple event storms may be more dangerous to power systems than single more extreme events. A power network does not distinguish events and, given its temporal sensitivity, would see the entire period as uninterrupted driving.

4 Pulsation appropriate GIC proxies

The time derivative of the disturbed B-field has long been used as a proxy for GIC activity, largely due to its importance in Faraday's law of induction that drives GICs (Viljanen et al., 2001). A large number of studies have compared the characteristics of GICs and dB/dt and found agreement (Viljanen, 1997) with one study even relating the one hour maxima of the two quantities through a power law in the time domain (Kataoka & Pulkkinen, 2008). A further improvement on the dB/dt proxy is the use of a rolling maximum of either 1 hour or 3 hours (Trichtchenko & Boteler, 2004) or more recently 30 minutes (Viljanen et al., 2015). These dB/dt proxies are useful as they do particularly well in resolving the SSC or substorm commencement periods, associated with large GIC values. In the frequency domain these impulses are characterised as broadband contributions, including frequencies higher than is typical for geomagnetic variation (upper bound of 0.5 Hz) (Simpson & Bahr, 2005).

A common misunderstanding is that dB/dt measured at Earth's surface drives the geoelectric field which drives GICs. In fact the entire induction loop that stretches deep into the Earth needs to be taken into account, with the result that the Earth modulates the disturbance dB/dt in the frequency domain and acts as a low-pass filter for this variation (Boteler & Pirjola, 2017). As a direct result, and taking into account the low-pass nature of the B-field itself, most of the GIC power sits below 50 mHz with lower frequencies carrying more weight (Oyedokun et al., 2020). The spectral peaks of pulsations sit on top of a '$1/f$' slope and this low-pass effect is ultimately why low-frequency pulsations couple to GICs so well.

Compared to GICs and the E-field, the dB/dt proxy is biased towards high-frequencies just as the B-field is biased towards low-frequencies in comparison. As briefly covered in Section 1, the power spectrum of the B-field follows a $1/f^m$ relation with frequency and dB/dt follows a $1/f^{m-2}$ relations, where $m - 2 \geq 0$. The E-field and GIC power spectra sit between these two responses, and hence dB/dt is biased to high-frequencies relative to the GICs of interest. In case of time domain B-field differencing used to estimate dB/dt, noise at the sampling rate can effectively drown out signals from low-frequency pulsations. For example let us assume $m = 2$, with the B-field power spectrum following a $1/f^2$ relation with frequency, dB/dt having a flat frequency response and GICs and the E-field having a $1/f$ relation. In this scenario let the sampling frequency be 1 Hz and

Figure 7. GIC frequency weighted proxy GIC_x at PAR during June 2015 storm that included the Ps6 type disturbance (upper panel). Since the lines at PAR are effectively north-south, only the GIC_x proxy is shown. Both the Ps6 pulsation, SSC and other low amplitude structures are captured. The time lag in signatures during Ps6 event is due to separation between FRD and PAR given a localized event. Middle panel shows traditional dB/dt at 1 s cadence which misses the pulsation event and low amplitude structures. Bottom panel shows the often used rolling 30 min dB/dt envelope which does better but also misses the pulsation event. Dashed black lines indicate 5 sigma from mean noise levels either GIC or proxies.

there be Pc5 pulsations of 150 s. For dB/dt, the ratio of frequency scaling between the pulsation frequency and Nyquist frequency is 1, whereas for the GIC spectrum it would be 75. For that same pulsation signal, the dB/dt signal would need to be 75 times stronger to be an accurate proxy for the GIC signal. Given longer period pulsations, such as the Ps6 type-disturbances seen at PAR, the effect is even larger. Ultimately, the high-frequency noise can drown out low-frequency pulsation signals. Peaks or spikes on the other hand are broadband driving and are adequately reproduced by dB/dt. When dealing with 1 minute cadence B-field data, the sampling rate is closer to the frequency of low-frequency pulsations and performs better than the 1 s cadence data, which is becoming more widely available as observatories modernise (Turbitt, 2014). Of course using too low a cadence for the same Pc5 pulsations, such as 5 minutes, will miss the pulsation activity entirely, as seen in Figure 2 with the Pc4 pulsation in 1 minute cadence data at GRS. Ideally, a pulsation effective proxy would have to match the relative weightings of the sampling rate's Nyquist frequency with the narrow-band pulsation's frequency. The proxy would further need to satisfy this condition for multiple pulsation bands.

632   A possible further manifestation of the high-frequency bias of dB/dt is the confu-
633 sion that arises in cases where the GIC profile looks more like the B-field than dB/dt
634 (Watari et al., 2009). As mentioned, the surface dB/dt field is not a true reflection of
635 the GIC driver and the Earth's conductivity structure needs to be taken into account.
636 Differences in the conductivity structure are often used as the explanation in cases where
637 confusion arises (Watari et al., 2009; Pirjola, 2010). In the more extreme case of the June
638 2015 storm presented in this paper, we see high correlation between GIC and dB/dt as
639 well as the B-field during different parts of the storm. As seen in Figure 3, during the
640 low-frequency Ps6 event, the B-field is representative of the GIC profile and shows sim-
641 ilar structure in period and phase. In Figure 7, we see that during the broadband SSC
642 of the same storm, dB/dt is representative of the GIC profile. The B-field intrinsically
643 has lower frequency components compared to dB/dt, especially at 1 s sampling cadence.
644 During a pulsation interval with a roughly 20 minute period, 1 s cadence dB/dt cannot
645 reproduce the variation required, as seen in the middle panel of Figure 7. For the im-
646 pulse during the SSC on the other hand, a higher cadence can better resolve the peak
647 and dB/dt with its higher frequency content does better. Similar results are seen with
648 other pulsations (see Figure 2) and up to now it has been fortuitous that 1 minute sam-
649 pling has more spectral weight (been more representative) than 1 s sampling. Given low-
650 frequency driving, whatever the Earth conductivity, a high sampling rate will not be sat-
651 isfactorily effective.

652   In the case of low-frequency driving and the modern standard of 1 s cadence B-field
653 data, instead of dB/dt a proxy akin to geoelectric field will be much more effective (Marshall
654 et al., 2010, 2011). In the frequency domain, the two components (directional projec-
655 tions) of the GIC proxy would be,

$$GIC_{x,y}(f) \quad \propto \quad \frac{1}{\sqrt{f}} Bdot_{y,x}(f), \tag{2}$$

656 where $Bdot$ refers to dB/dt and the orthogonality between driving and induced compo-
657 nents is explicitly absorbed. The B-field or dB/dt can be used interchangeably, since they
658 linked in the frequency domain by $2\pi i$. dB/dt does however have the benefit of being
659 centred about zero and no baseline subtraction is needed when applying the FFT. Tak-
660 ing the inverse FFT gets the resulting proxy for each component in the time domain. A
661 normalised version of the GIC proxy defined by Marshall et al. (2011) can be used to es-
662 timate levels of GIC risk (Marshall et al., 2011; Zhang et al., 2016; Tozzi et al., 2019).
663 The focus here is rather on replicating pulsations in a GIC proxy and (2) is applied as
664 is. In Figure 7 only the GIC_x proxy that is related to the B_y component is shown as the
665 network is north-south effective at PAR. In all subfigures, the 5 sigma noise level of the
666 parameters during quiet time is indicated with horizontal dashed lines, with overlap in
667 some cases. Any proxy used should aim to characterise signals well when above this level.
668 The $GIC_{x,y}$ proxy effectively takes into account the low-pass frequency weighting needed
669 to reproduce measured GIC across all frequencies, adhering to where GIC power sits in-
670 dependent of sampling rate and doing significantly better than the other proxies. Although
671 it looks very similar to the derivation of the geoelectric field for a homogeneous Earth
672 it should be stressed that $GIC_{x,y}$ is just a frequency weighted proxy with no further scal-
673 ing. In such a way even long period pulsations can be identified with other pulsations
674 and impulses in a single proxy using high cadence data. Standardising the proxy with
675 no further scaling means the proxy is comparable for different events and stations. Ul-
676 timately, different events can be characterised using this common proxy for different sta-
677 tions, similar to SYM-H, and relative storm strengths quantified across frequencies and
678 conductivity regions in such a way. Taking into account the cumulative proxy is also of
679 interest as it can identify possible degradation risk (Lotz & Danskin, 2017; Moodley &
680 Gaunt, 2017).

5 Conclusions

Although pulsations have been acknowledged as sources of GIC driving and are used extensively as signal sources for magnetotelluric sounding (Simpson & Bahr, 2005) in the geophysical step of GIC modelling, the extent of their contribution has often not been recognised, especially at mid-latitudes where population density, and therefore power network coverage, peaks. In this paper pulsation signatures linked to geomagnetic pulsations were identified in measured mid-latitude GIC data during intense and extreme geomagnetic storms. The coupling and amplitude of GIC associated with pulsations is proportional to the period making low-frequency pulsations significant. Given two pulsations of the same amplitude, the longer period pulsation will couple more efficiently and drive larger GICs. As such peak dB/dt is not the ultimate proxy for GIC-related damage, as efficient coupling during pulsating intervals can occur while dB/dt is moderate. We've shown that this can drive significant GIC at a mid-latitude network during intense geomagnetic storms.

Specifically, two geomagnetic storms that had low-frequency oscillations in the Pc5 and Ps6 bands were observed to couple to significant measured GICs at mid-latitude locations. A third storm, used for regulatory benchmarking, found similar Pc5 coupling in the derived geoelectric field, which ultimately drives GICs. The characteristics of the two pulsation types seen are very different. Global Pc5 events tend to be associated with superstorms or multiple CME storms and affect the entire globe. The H component of the B-field is dominant and east-west nodes in power networks are more at risk. Larger amplitude Ps6 events on the other hand are associated with substorms and are not as dependent on storm intensity, although coinciding with geomagnetic storm minimum may make them more effective, with the effect of their FACs driving GIC in mid-latitudes. These events are also more spatially localised and restricted from the pre-midnight to morning sectors, although they have associated drift and may last a number of hours. The dominant D component in turn means north-south nodes in power networks are more at risk.

Storm time global Pc5 pulsations were found to generate significant GIC or GIC effective geoelectric fields in the famous superstorms of 1989 and 2003, reaching amplitudes between a quarter and two thirds of those at the SSC for extended periods of over an hour. An intense Ps6-type substorm associated disturbance occurring during the 22–23 June 2015 geomagnetic storm was shown to be a widespread event that covered most of the eastern North America. This event caused GICs of about 10 A at regular 20 minute intervals over a 2 and a half hour period at a mid-latitude station not previously thought to be affected by Ps6 disturbances. The sustained cumulative GIC pulsation driving as measured by RMS over a two hour period exceeded that of the two hour period including the SSC and main phase onset by 10%. At higher latitudes or in different networks these effects can possibly be larger, as has been shown in the Kola peninsula (Apatenkov et al., 2020). Ps6 disturbances are more a function of magnetosphere loading, with the challenging prediction of the magnetotail and substorm environment, along with fine structures in the near-Earth current systems, required for an operational lead time useful to utilities.

From an engineering aspect, both the Pc5 and Ps6 types of pulsations induce significant low-frequency GICs that cannot be modelled accurately using only a dc assumption. For more representative and realistic modelling of the stress to transformers and the power system, a driving ac current with frequencies up to the Pc5 pulsation band (6.7 mHz) is needed. Such modelling is distinctly different to dc modelling and would already be needed if the NERC benchmark profile were applied explicitly, since there is Pc5 driving in the benchmark March 1989 storm. The direct damage caused by pulsations is not the same as that of peak currents, but may contribute to voltage instability, initiate insulation degradation and cause corrosion in pipelines. A further consid-

eration is that pulsation driving typically occurs after the SSC peak GIC and often in the recovery phase when the system is already under stress.

When considering pulsations, the typical dB/dt proxy widely used no longer describes active periods when the pulsation period is significantly different from the sampling period of the B-field. This is evident in the June 2015 storm, where a Ps6 pulsation interval with a period of over 20 minutes was not identified in either 1 s cadence dB/dt or a rolling max window derived from 1 s cadence dB/dt. A frequency weighted proxy that captures the low-pass filter effect of the Earth's conductivity on dB/dt has been shown to capture pulsation activity in multiple bands adequately.

References

Amm, O., Aksnes, A., Stadsnes, J., Østgaard, N., Vondrak, R., Germany, G., . . . Viljanen, A. (2005). Mesoscale ionospheric electrodynamics of omega bands determined from ground-based electromagnetic and satellite optical observations. *Annales Geophysicae*, *23*(2), 325–342. doi: 10.5194/angeo-23-325-2005

Apatenkov, S. V., Pilipenko, V. A., Gordeev, E. I., Viljanen, A., Juusola, L., Belakhovsky, V. B., . . . Selivanov, V. N. (2020). Auroral Omega Bands are a Significant Cause of Large Geomagnetically Induced Currents. *Geophysical Research Letters*, *47*(6). doi: 10.1029/2019GL086677

Apatenkov, S. V., Sergeev, V. A., Pirjola, R., & Viljanen, A. (2004). Evaluation of the geometry of ionospheric current systems related to rapid geomagnetic variations. *Annales Geophysicae*, *22*(1), 63–72. doi: 10.5194/angeo-22-63-2004

Balasis, G., Daglis, I. A., Mann, I. R., Papadimitriou, C., Zesta, E., Georgiou, M., . . . Tsinganos, K. (2015). Multi-satellite study of the excitation of Pc3 and Pc4-5 ULF waves and their penetration across the plasmapause during the 2003 Halloween superstorm. *Annales Geophysicae*, *33*(10), 1237–1252. doi: 10.5194/angeo-33-1237-2015

Belakhovsky, V., Pilipenko, V., Engebretson, M., Sakharov, Y., & Selivanov, V. (2019). Impulsive disturbances of the geomagnetic field as a cause of induced

currents of electric power lines. *Journal of Space Weather and Space Climate*, *9*, A18. doi: 10.1051/swsc/2019015

Bolduc, L. (2002). GIC observations and studies in the Hydro-Québec power system. *Journal of Atmospheric and Solar-Terrestrial Physics*, *64*(16), 1793–1802. doi: 10.1016/S1364-6826(02)00128-1

Boteler, D. H. (2015). The Evolution of Québec Earth Models Used to Model Geomagnetically Induced Currents. *IEEE Transactions on Power Delivery*, *30*(5), 2171–2178. doi: 10.1109/TPWRD.2014.2379260

Boteler, D. H. (2019). A 21st Century View of the March 1989 Magnetic Storm. *Space Weather*, *17*(10), 1427–1441. doi: 10.1029/2019SW002278

Boteler, D. H., & Pirjola, R. J. (2017). Modeling geomagnetically induced currents. *Space Weather*, *15*(1), 258–276. doi: 10.1002/2016SW001499

Cagniard, L. (1953). Basic Theory of the Magneto-Telluric Method of Geophysical Prospecting. *GEOPHYSICS*, *18*(3), 605–635. doi: 10.1190/1.1437915

Cheng, C.-C., Mann, I. R., & Baumjohann, W. (2014). Association of consecutive Pi2-Ps6 band pulsations with earthward fast flows in the plasma sheet in response to IMF variations. *Journal of Geophysical Research: Space Physics*, *119*(5), 3617–3640. doi: 10.1002/2013JA019275

Connors, M., Rostoker, G., Sofko, G., McPherron, R. L., & Henderson, M. G. (2003). Ps 6 disturbances: relation to substorms and the auroral oval. *Annales Geophysicae*, *21*(2), 493–508. doi: 10.5194/angeo-21-493-2003

de Villiers, J. S., Kosch, M., Yamazaki, Y., & Lotz, S. (2017). Influences of various magnetospheric and ionospheric current systems on geomagnetically induced currents around the world. *Space Weather*, *15*(2), 403–417. doi: 10.1002/2016SW001566

Divett, T., Richardson, G. S., Beggan, C. D., Rodger, C. J., Boteler, D. H., Ingham, M., ... Dalzell, M. (2018). Transformer-Level Modeling of Geomagnetically Induced Currents in New Zealand's South Island. *Space Weather*, *16*(6), 718–735. doi: 10.1029/2018SW001814

Federal Energy Regulatory Commission: Reliability Standard for Transmission System Planned Performance for Geomagnetic Disturbance Events. Order 830. (Sep 2016, Washington DC). `https://www.ferc.gov/whats-new/comm-meet/2016/092216/E-4.pdf`.

Gaunt, C. T., & Coetzee, G. (2007). Transformer failures in regions incorrectly considered to have low GIC-risk. In *2007 IEEE Lausanne Power Tech* (pp. 807–812). IEEE. doi: 10.1109/PCT.2007.4538419

Gjerloev, J. W. (2012). The SuperMAG data processing technique. *Journal of Geophysical Research: Space Physics*, *117*(A9). doi: 10.1029/2012JA017683

Gonzalez, W. D., Joselyn, J. A., Kamide, Y., Kroehl, H. W., Rostoker, G., Tsurutani, B. T., & Vasyliunas, V. M. (1994). What is a geomagnetic storm? *Journal of Geophysical Research*, *99*(A4), 5771. doi: 10.1029/93JA02867

Hejda, P., & Bochníček, J. (2005). Geomagnetically induced pipe-to-soil voltages in the Czech oil pipelines during October-November 2003. *Annales Geophysicae*, *23*(9), 3089–3093. doi: 10.5194/angeo-23-3089-2005

Henderson, M. G., Kepko, L., Spence, H. E., Connors, M., Sigwarth, J. B., Frank, L. A., ... Yumoto, K. (2002). The evolution of north-south aligned auroral forms into auroral torch structures: the generation of omega bands and Ps6 pulsations via flow bursts. In *6th International Conference on Substorms* (pp. 1–6). doi: 10.13140/RG.2.1.4976.9688

Jankee, P., Chisepo, H., Adebayo, V., Oyedokun, D., & Gaunt, C. T. (2020). Transformer models and meters in MATLAB and PSCAD for GIC and leakage dc studies. In *2020 International SAUPEC/RobMech/PRASA Conference* (pp. 1–6). IEEE. doi: 10.1109/SAUPEC/RobMech/PRASA48453.2020.9041060

Kappenman, J. G. (2005). An overview of the impulsive geomagnetic field disturbances and power grid impacts associated with the violent Sun-Earth connec-

tion events of 29-31 October 2003 and a comparative evaluation with other contemporary storms. *Space Weather*, *3*(8). doi: 10.1029/2004SW000128

Kataoka, R., & Pulkkinen, A. (2008). Geomagnetically induced currents during intense storms driven by coronal mass ejections and corotating interacting regions. *Journal of Geophysical Research: Space Physics*, *113*(A3). doi: 10.1029/2007JA012487

Khawaja, R. H., & Blackburn, T. R. (2009). Impact of high temperature on partial discharges in oil-impregnated insulation. In *2009 Australasian Universities Power Engineering Conference* (p. 1-6). IEEE. Retrieved from `https:// ieeexplore.ieee.org/document/5356639`

Kozyreva, O., Pilipenko, V., Krasnoperov, R., Baddeley, L., Sakharov, Y., & Dobrovolsky, M. (2019). Fine structure of substorm and geomagnetically induced currents. *Annals of Geophysics*, *62*. doi: 10.4401/ag-8198

Le, G., Cai, Z., Wang, H., & Zhu, Y. (2012). Solar cycle distribution of great geomagnetic storms. *Astrophysics and Space Science*, *339*(1), 151–156. doi: 10 .1007/s10509-011-0960-y

Lehtinen, M., & Pirjola, R. (1985). Currents produced in earthed conductor networks by geomagnetically-induced electric fields. *Annales Geophysicae*, *3*(4), 479–484.

Lotz, S. I., & Danskin, D. W. (2017). Extreme Value Analysis of Induced Geoelectric Field in South Africa. *Space Weather*, *15*(10), 1347–1356. doi: 10.1002/ 2017SW001662

Lühr, H., & Schlegel, K. (1994). Combined measurements of EISCAT and the EISCAT magnetometer cross to study Ω bands. *Journal of Geophysical Research*, *99*(A5), 8951. doi: 10.1029/94JA00487

Marin, J., Pilipenko, V., Kozyreva, O., Stepanova, M., Engebretson, M., Vega, P., & Zesta, E. (2014). Global Pc5 pulsations during strong magnetic storms: excitation mechanisms and equatorward expansion. *Annales Geophysicae*, *32*(4), 319–331. doi: 10.5194/angeo-32-319-2014

Marshall, R. A., Smith, E. A., Francis, M. J., Waters, C. L., & Sciffer, M. D. (2011). A preliminary risk assessment of the Australian region power network to space weather. *Space Weather*, *9*(10), 1–18. doi: 10.1029/2011SW000685

Marshall, R. A., Waters, C. L., & Sciffer, M. D. (2010). Spectral analysis of pipe-to-soil potentials with variations of the Earth's magnetic field in the Australian region. *Space Weather*, *8*(5). doi: 10.1029/2009SW000553

Moodley, N., & Gaunt, C. T. (2017). Low Energy Degradation Triangle for power transformer health assessment. *IEEE Transactions on Dielectrics and Electrical Insulation*, *24*(1), 639–646. doi: 10.1109/TDEI.2016.006042

Nakamura, R., Sergeev, V. A., Baumjohann, W., Plaschke, F., Magnes, W., Fischer, D., . . . Saito, Y. (2016). Transient, small-scale field-aligned currents in the plasma sheet boundary layer during storm time substorms. *Geophysical Research Letters*, *43*(10), 4841–4849. doi: 10.1002/2016GL068768

Newell, P. T., & Gjerloev, J. W. (2011). Evaluation of SuperMAG auroral electrojet indices as indicators of substorms and auroral power. *Journal of Geophysical Research: Space Physics*, *116*(A12). doi: 10.1029/2011JA016779

Ngwira, C. M., Habarulema, J., Astafyeva, E., Yizengaw, E., Jonah, O. F., Crowley, G., . . . Coffey, V. (2019). Dynamic Response of Ionospheric Plasma Density to the Geomagnetic Storm of 22-23 June 2015. *Journal of Geophysical Research: Space Physics*, *124*(8), 7123–7139. doi: 10.1029/2018JA026172

Ngwira, C. M., McKinnell, L.-A., Cilliers, P. J., Viljanen, A., & Pirjola, R. (2009). Limitations of the modeling of geomagnetically induced currents in the South African power network. *Space Weather*, *7*(10). doi: 10.1029/2009SW000478

Oyedokun, D., Heyns, M., Cilliers, P., & Gaunt, C. (2020). Frequency Components of Geomagnetically Induced Currents for Power System Modelling. In *2020 International SAUPEC/RobMech/PRASA Conference* (pp. 1–6). IEEE. doi: 10

.1109/SAUPEC/RobMech/PRASA48453.2020.9041021

Paxton, L. J., Meng, C.-I., Fountain, G. H., Ogorzalek, B. S., Darlington, E. H., Gary, S. A., ... Smith, B. E. (1992). Special sensor ultraviolet spectrographic imager: An instrument description. In S. Chakrabarti & A. B. Christensen (Eds.), *Instrumentation for Planetary and Terrestrial Atmospheric Remote Sensing* (pp. 2–15). International Society for Optics and Photonics. doi: 10.1117/12.60595

Paxton, L. J., Meng, C.-I., Fountain, G. H., Ogorzalek, B. S., Darlington, E. H., Gary, S. A., ... Daniell, Jr., R. E. (1993). SSUSI: Horizon-to-horizon and limb-viewing spectrographic imager for remote sensing of environmental parameters. In R. E. Huffman (Ed.), *Ultraviolet Technology IV* (pp. 161–176). International Society for Optics and Photonics. doi: 10.1117/12.140846

Paxton, L. J., Schaefer, R. K., Zhang, Y., & Kil, H. (2017). Far ultraviolet instrument technology. *Journal of Geophysical Research: Space Physics*, *122*(2), 2706–2733. doi: 10.1002/2016JA023578

Pilipenko, V., Kozyreva, O., Belakhovsky, V., Engebretson, M. J., & Samsonov, S. (2010). Generation of magnetic and particle Pc5 pulsations during the recovery phase of strong magnetic storms. *Proceedings of the Royal Society A: Mathematical, Physical and Engineering Sciences*, *466*(2123), 3363–3390. doi: 10.1098/rspa.2010.0079

Pirjola, R. (2010). Derivation of characteristics of the relation between geomagnetic and geoelectric variation fields from the surface impedance for a two-layer earth. *Earth, Planets and Space*, *62*(3), 287–295. doi: 10.5047/eps.2009.09.002

Potapov, A., Guglielmi, A., Tsegmed, B., & Kultima, J. (2006). Global Pc5 event during 29-31 October 2003 magnetic storm. *Advances in Space Research*, *38*(8), 1582–1586. doi: 10.1016/j.asr.2006.05.010

Pulkkinen, A., & Kataoka, R. (2006). S-transform view of geomagnetically induced currents during geomagnetic superstorms. *Geophysical Research Letters*, *33*(12). doi: 10.1029/2006GL025822

Pulkkinen, A., Lindahl, S., Viljanen, A., & Pirjola, R. (2005). Geomagnetic storm of 29-31 October 2003: Geomagnetically induced currents and their relation to problems in the Swedish high-voltage power transmission system. *Space Weather*, *3*(8). doi: 10.1029/2004SW000123

Pulkkinen, A., Thomson, A., Clarke, E., & McKay, A. (2003). April 2000 geomagnetic storm: ionospheric drivers of large geomagnetically induced currents. *Annales Geophysicae*, *21*(3), 709–717. doi: 10.5194/angeo-21-709-2003

Reiff, P. H., Daou, A. G., Sazykin, S. Y., Nakamura, R., Hairston, M. R., Coffey, V., ... Genestreti, K. J. (2016). Multispacecraft observations and modeling of the 22/23 June 2015 geomagnetic storm. *Geophysical Research Letters*, *43*(14), 7311–7318. doi: 10.1002/2016GL069154

Rostoker, G., & Barichello, J. C. (1980). Seasonal and diurnal variation of Ps 6 magnetic disturbances. *Journal of Geophysical Research: Space Physics*, *85*(A1), 161–163. doi: 10.1029/JA085iA01p00161

Saito, T. (1969). Geomagnetic pulsations. *Space Science Reviews*, *10*(3). doi: 10.1007/BF00203620

Saito, T. (1978). Long-period irregular magnetic pulsation, Pi3. *Space Science Reviews*, *21*(4), 211–212. doi: 10.1007/BF00173068

Sakurai, T., & Tonegawa, Y. (2005). Extreme magnetic field variations during the October 2003 superstorm. *Advances in Polar Upper Atmosphere Research*(19), 21–41.

Simpson, F., & Bahr, K. (2005). *Practical Magnetotellurics*. Cambridge: Cambridge University Press. doi: 10.1017/CBO9780511614095

Smith, A. W., Freeman, M. P., Rae, I. J., & Forsyth, C. (2019). The Influence of Sudden Commencements on the Rate of Change of the Surface Horizontal

Magnetic Field in the United Kingdom. *Space Weather*, *17*(11), 1605–1617. doi: 10.1029/2019SW002281

Sokolova, E. Y., Kozyreva, O. V., Pilipenko, V. A., Sakharov, Y. A., & Epishkin, D. V. (2019). Space-Weather-Driven Geomagnetic- and Telluric-Field Variability in Northwestern Russia in Correlation with Geoelectrical Structure and Currents Induced in Electric-Power Grids. *Izvestiya, Atmospheric and Oceanic Physics*, *55*(11), 1639–1658. doi: 10.1134/S000143381911015X

Stephenson, J. A. E., & Walker, A. D. M. (2002). HF radar observations of Pc5 ULF pulsations driven by the solar wind. *Geophysical Research Letters*, *29*(9), 81–84. doi: 10.1029/2001GL014291

Tozzi, R., De Michelis, P., Coco, I., & Giannattasio, F. (2019). A Preliminary Risk Assessment of Geomagnetically Induced Currents over the Italian Territory. *Space Weather*, *17*(1), 46–58. doi: 10.1029/2018SW002065

TPL-007-1: Transmission System Planned Performance for Geomagnetic Disturbance Events. (North American Reliability Corp., 2017.). `https://www.nerc.com/pa/Stand/Reliability%20Standards/TPL-007-1.pdf`.

Trichtchenko, L., & Boteler, D. (2004). Modeling Geomagnetically Induced Currents Using Geomagnetic Indices and Data. *IEEE Transactions on Plasma Science*, *32*(4), 1459–1467. doi: 10.1109/TPS.2004.830993

Tsurutani, B. T., Hajra, R., Echer, E., & Gjerloev, J. W. (2015). Extremely intense (SML≤ −2500 nT) substorms: isolated events that are externally triggered? *Annales Geophysicae*, *33*(5), 519–524. doi: 10.5194/angeo-33-519-2015

Turbitt, C. (2014). *INTERMAGNET Technical Note TN6: INTERMAGNET Definitive One-second Data Standard.* `https://intermagnet.org/publications/im_tn_06_v1_0.pdf`.

Viljanen, A. (1997). The Relation Between Geomagnetic Variations and Their Time Derivatives and Implications for Estimation of Induction Risks. *Geophysical Research Letters*, *24*(6), 631–634. doi: 10.1029/97GL00538

Viljanen, A., Amm, O., & Pirjola, R. (1999). Modeling geomagnetically induced currents during different ionospheric situations. *Journal of Geophysical Research: Space Physics*, *104*(A12), 28059–28071. doi: 10.1029/1999JA900337

Viljanen, A., Nevanlinna, H., Pajunpää, K., & Pulkkinen, A. (2001). Time derivative of the horizontal geomagnetic field as an activity indicator. *Annales Geophysicae*, *19*(9), 1107–1118. doi: 10.5194/angeo-19-1107-2001

Viljanen, A., Wintoft, P., & Wik, M. (2015). Regional estimation of geomagnetically induced currents based on the local magnetic or electric field. *Journal of Space Weather and Space Climate*, *5*, A24. doi: 10.1051/swsc/2015022

Villante, U., Vellante, M., de Lauretis, M., Meloni, A., & Palangio, P. (1990). The strong geomagnetic storm of March 13, 1989 - An analysis at a low latitude station. *Annales Geophysicae*, *8*(5), 337–342.

Walker, A. D. M. (2005). Excitation of field line resonances by sources outside the magnetosphere. *Annales Geophysicae*, *23*(10), 3375–3388. doi: 10.5194/angeo-23-3375-2005

Watari, S., Kunitake, M., Kitamura, K., Hori, T., Kikuchi, T., Shiokawa, K., . . . Tsuneta, Y. (2009). Measurements of geomagnetically induced current in a power grid in Hokkaido, Japan. *Space Weather*, *7*(3). doi: 10.1029/2008SW000417

Wild, J. A., Woodfield, E. E., Donovan, E., Fear, R. C., Grocott, A., Lester, M., . . . Björnsson, G. (2011). Midnight sector observations of auroral omega bands. *Journal of Geophysical Research: Space Physics*, *116*(A5), 1–20. doi: 10.1029/2010JA015874

Wild, J. A., Yeoman, T. K., Eglitis, P., & Opgenoorth, H. J. (2000). Multi-instrument observations of the electric and magnetic field structure of omega bands. *Annales Geophysicae*, *18*(1), 99–110. doi: 10.1007/s00585-000-0099-6

Yagova, N. V., Pilipenko, V. A., Fedorov, E. N., Lhamdondog, A. D., & Gusev, Y. P. (2018). Geomagnetically Induced Currents and Space Weather: Pi3 Pulsations and Extreme Values of Time Derivatives of the Geomagnetic Field's Horizontal Components. *Izvestiya, Physics of the Solid Earth*, *54*(5), 749–763. doi: 10.1134/S1069351318050130

Zhang, J. J., Wang, C., Sun, T. R., & Liu, Y. D. (2016). Risk assessment of the extreme interplanetary shock of 23 July 2012 on low-latitude power networks. *Space Weather*, *14*(3), 259–270. doi: 10.1002/2015SW001347